

LA-UR-20-24383 (Accepted Manuscript)

## Radiation Belt Response to Fast Reverse Shock at Geosynchronous Orbit

Bhaskar, Ankush  
Sibeck, David G.  
Kanekal, Shrikhanth G.  
Singer, H. J.  
Reeves, Geoffrey D.  
Oliveira, D. M.  
Kang, S. K.

Provided by the author(s) and the Los Alamos National Laboratory (2021-11-19).

**To be published in:** The Astrophysical Journal

**DOI to publisher's version:** 10.3847/1538-4357/abd702

**Permalink to record:** <http://permalink.lanl.gov/object/view?what=info:lanl-repo/lareport/LA-UR-20-24383>

**Disclaimer:**

Los Alamos National Laboratory, an affirmative action/equal opportunity employer, is operated by Triad National Security, LLC for the National Nuclear Security Administration of U.S. Department of Energy under contract 89233218CNA000001. By approving this article, the publisher recognizes that the U.S. Government retains nonexclusive, royalty-free license to publish or reproduce the published form of this contribution, or to allow others to do so, for U.S. Government purposes. Los Alamos National Laboratory requests that the publisher identify this article as work performed under the auspices of the U.S. Department of Energy. Los Alamos National Laboratory strongly supports academic freedom and a researcher's right to publish; as an institution, however, the Laboratory does not endorse the viewpoint of a publication or guarantee its technical correctness.



# Radiation Belt Response to Fast Reverse Shock at Geosynchronous Orbit

Ankush Bhaskar<sup>1,2,3</sup>, David Sibeck<sup>1</sup>, Shrikanth G. Kanekal<sup>1</sup>, Howard J. Singer<sup>4</sup>, Geoffrey Reeves<sup>5</sup>, Denny M. Oliveira<sup>1,6</sup>, Suk-Bin Kang<sup>1</sup>, and Colin Komar<sup>1</sup>

<sup>1</sup> NASA/Goddard Space Flight Center, Greenbelt, MD, USA; ankushbhaskar@gmail.com

<sup>2</sup> University Corporation for Atmospheric Research, Boulder, USA

<sup>3</sup> Space Physics Laboratory, Vikram Sarabhai Space Centre, Thiruvananthapuram, India

<sup>4</sup> NOAA-Space Weather Prediction Center, CO, USA

<sup>5</sup> Los Alamos National Laboratory, NM, USA

<sup>6</sup> Goddard Planetary Heliophysics Institute, University of Maryland, Baltimore, USA

Received 2020 December 1; revised 2020 December 23; accepted 2020 December 25; published 2021 MM DD

## Abstract

Fast reverse shocks (FRSs) cause the magnetosphere to expand, by contrast to the well-known compressions caused by the impact of fast forward shocks (FFSs). Usually, FFSs are more geoeffective than FRSs, and consequently the inner magnetosphere dynamic responses to both shock types can be quite different. In this study, we investigate for the first time the radiation belt response to an FRS impact using multi-satellite observations and numerical simulations. Spacecraft on the dayside observed decreases in magnetic field strength and energetic ( $\sim 40$ – $475$  keV) particle fluxes. Timing analysis shows that the magnetic field signature propagated from the dayside to the nightside magnetosphere. Particles with different energies vary simultaneously at each spacecraft, implying a non-dispersive particle response to the shock. Spacecraft located at lower L-shells did not record any significant signatures. The observations indicate a local time dependence of the response associated with the shock inclination, with the clearest signatures being observed in the dusk–midnight sector. Simulations underestimate the amplitude of the magnetic field variations observed on the nightside. The observed decreases in the electron intensities result from a combination of radial gradient and adiabatic effects. The radial gradients in the spectral index appear to be the dominant contributor to the observed variations of electrons seen on the dayside (near noon and dusk) and on the nightside (near midnight). This study shows that even an FRS can affect the radiation belts significantly and provides an opportunity to understand their dynamic response to a sudden expansion of the magnetosphere.

*Unified Astronomy Thesaurus concepts:* Fast solar wind (1872); Van Allen radiation belt (1758); Planetary magnetosphere (997); Interplanetary particle acceleration (826); Solar wind (1534); Interplanetary magnetic fields (824); Interplanetary discontinuities (820); Solar-planetary interactions (1472); Magnetohydrodynamical simulations (1966); Solar activity (1475); Solar-terrestrial interactions (1473);

## 1. Introduction

Interplanetary (IP) shocks are a frequent feature of the solar wind (Burlaga 1971; Richter et al. 1985). Fast mode IP shocks occur when the relative speed between the ambient solar wind and the shock speed is larger than the local magnetosonic speed (Landau & Lifshitz 1960; Richter et al. 1985; Tsurutani et al. 2011; Oliveira 2017). Fast IP shocks that are moving away from the Sun are classified as fast forward shocks (FFSs), while fast shocks that propagate toward the Sun are classified as fast reverse shocks (FRSs) (Burlaga 1995; Tsurutani et al. 2011; Oliveira 2017). Similarly to FFSs, FRSs are carried antisunward by the continuous solar wind flow as seen from a reference frame defined as a spacecraft in the IP space or the Earth itself (Richter et al. 1985; Burlaga 1995; Tsurutani et al. 2011; Oliveira 2017; Oliveira & Samsonov 2018). FFSs are more numerous during solar maxima, while FRS occurrence rates have no clear correlation with solar activity (Echer et al. 2003; Kilpua et al. 2015; Cavus et al. 2019). Kilpua et al. (2015) showed that the occurrence rates of FFSs are higher than the occurrence rates of FRSs during all solar phases, except during solar minima.

The steepening conditions across the fronts of FFSs and FRSs are different. In the case of FFSs, all plasma parameters (particle number density, thermal temperature, and velocity), along with the interplanetary magnetic field (IMF) increase.

Conversely, in the case of FRSs, all solar wind and IMF parameters decrease, except the solar wind plasma velocity (Landau & Lifshitz 1960; Burlaga 1971; Richter et al. 1985; Burlaga 1995; Burguess 1995; Tsurutani et al. 2011). See Figure 2 of Oliveira (2017) for comparisons between schematic profiles of FFSs and FRSs. These distinct shock conditions are responsible for different magnetospheric responses to the impacts of FFSs and FRSs. For CIRs at 1 au, there are often reverse shocks without forward shocks. However, at large distances from the Sun all CIRs typically have both forward and reverse shocks (Smith & Wolfe 1976). Moreover, FRSs are found to be more efficient in accelerating the particles in interplanetary space as compared to FFSs (Tsurutani et al. 1982). It is therefore important to study the impact of FRSs on the magnetosphere and radiation belt.

FFSs are known to be the most geoeffective class of IP shocks (Echer et al. 2004; Alves et al. 2011; Tsurutani et al. 2011; Oliveira & Raeder 2015; Oliveira & Samsonov 2018). The first and most dramatic magnetospheric response to the impact of FFSs are characterized by positive sudden impulses ( $SI^+$ ) in the horizontal component of the geomagnetic field measured by magnetometers located in the space (Patel & Coleman 1970; Huttunen et al. 2005; Wang et al. 2010; Su et al. 2015; Rudd et al. 2019) and on the ground (Siscoe et al. 1968; Smith et al. 1986; Takeuchi et al. 2002b; Rudd et al. 2019), as a consequence of a sudden increase of the solar wind

dynamic pressure (Russell et al. 1994a, 1994b; Echer et al. 2005; Wang et al. 2010; Rudd et al. 2019). The impact of FFS can even trigger daytime aurora and nightside supersubstorms (Zhou & Tsurutani 1999; Tsurutani et al. 2001; Zhou & Tsurutani 2001; Hajra & Tsurutani 2018). On the other hand, in the case of FRSs, the sudden impulse response is negative ( $SI^-$ ) as geospace and ground magnetometers observe negative excursions in the horizontal component of the geomagnetic field (Akasofu 1964; Takeuchi et al. 2002a; Andrioli et al. 2006; Zhang et al. 2010). This is due to magnetospheric expansions caused by solar wind dynamic pressure decreases such as those associated with FRS/solar wind discontinuity impacts (Joselyn & Tsurutani 1990; Araki 1994; Zhang et al. 2010; Vichare et al. 2014). Moreover, Hajra et al. (2020) showed that FRSs which occur during geomagnetic storms cause recoveries in geomagnetic activity.

The impact of strong shocks can inject and energize particles into the radiation belts resulting in transient variation of the particle intensities. The classic example of such events is the strongest  $SI^+$  recorded, which occurred on 1991 March 24 (Araki et al. 1997). The shock associated with this  $SI^+$  formed a double-peaked inner radiation belt which lasted for years (Mullen et al. 1991; Looper et al. 1994). The radiation belt electron and proton responses to shocks have been simulated by Li et al. (1993) and Hudson et al. (1995). Their simulation results showed that electrons of few MeV were transported from  $L > 6$  to  $L \sim 2.5$  by an inductive electric field which energizes them up to 40 MeV. A study by Kanekal et al. (2016) showed that ultrarelativistic electrons with energies  $> 6$  MeV were injected deep into the magnetosphere at  $L \sim 3$  within  $\sim 2$  minutes following the 2015 March 17 IP shock impact. Schiller et al. (2016) carried out a statistical study of highly relativistic electron injections caused by IP shock interactions with the magnetosphere. They observed that not all their shocks show signatures in MeV electrons; around 25% of IP shocks are associated with prompt MeV electron energization, and 14% are associated with prompt MeV electron depletions. Moreover, Zhang et al. (2018) studied shock-induced electric fields caused by IP shocks and suggested implications of these impulsive electric fields to the acceleration and transport of radiation belt electrons. Note that the processes responsible for the enhanced/depleted intensities of energetic particles within the magnetosphere following shock impacts can be understood in terms of some combination of (i) enhanced particle source populations or their radial transport and (ii) localized acceleration. Although intense shocks are relatively rare, their impact on the inner radiation belt can last for years or even decades. Therefore, they cannot be ignored in space weather and space technology related studies.

As can be seen, there has been considerable interest in studying the magnetospheric effects of  $SI^+$ s (caused by FFSs), but FRS interactions with radiation belt have received less attention. Just as a compression of the magnetosphere due to FFSs results in various transient processes, a sudden rarefaction due to FRSs or solar wind discontinuities can also generate interesting dynamics like generation of transient currents in magnetosphere and ionosphere (Vichare et al. 2014; Shen et al. 2017). There are various studies reporting on the geomagnetic field response to  $SI^-$ ; however, to the best of our knowledge there is no comprehensive study of the radiation belt response to FRSs.

This gap in understanding motivates the present study to investigate an FRS impact on the outer radiation belt in detail. Although shock impact has been studied extensively using spacecraft observations and simulations, there are at least three important problems which still need attention: (i) reverse shocks affect the radiation belts significantly? (ii) Do the impacts of reverse shocks on the inner and outer radiation belts simply mirror those of a forward shocks? (iii) What are the primary drivers (or causes) responsible for transient variations in particle fluxes during the shocks? To address these questions, the present study carries out multi-point spacecraft observations to evaluate and compare the outer radiation belt responses to the rarefaction of the magnetosphere during the transit of a reverse shock across the Earth's magnetosphere. The observed variations in electron and proton fluxes are interpreted based on our current understanding of particle dynamics in the magnetosphere.

The arrival of FRSs at the Earth is also associated with particle variations at certain locations in the magnetosphere during and after the shock passage. Intensification of high energy particle fluxes in the radiation belt affect orbiting communication and navigation satellites adversely. If a high-intensity shock similar to the event of 1991 March 24 occurs in the near future, its impact on space technology will be severe. The current study shows that even FRSs can affect radiation belt particles even though they are generally weaker than FFSs. The results from this study will assist in the better understanding of underlying physical processes and prediction of particle variations induced by FRS interactions with the Earth's magnetosphere. The study has further implications to shock-induced processes in other planetary magnetospheres of the solar system and exoplanets.

## 2. Data and Methods

We examined the interplanetary shock lists available at (<http://ipshocks.fi/database>) and ([https://www.cfa.harvard.edu/shocks/ac\\_master\\_data/ac\\_master\\_2014.html](https://www.cfa.harvard.edu/shocks/ac_master_data/ac_master_2014.html)) to identify FRSs from 2013 to 2016, an interval when high quality continuous data were available from the Van Allen Probes and other spacecraft.

There were a total of 29 FRSs during this period. Here we present a detailed case study of the single strongest event on the list which occurred in the declining phase of solar cycle 24. The driver of the shock is identified as a CIR. There is no fast forward shock associated with this CIR. It is known that CIRs are more frequent during the declining phase of the solar cycle (Tsurutani et al. 1995). This FRS was observed by the Wind spacecraft, on 2014 December 6, at 21:09 UT, the spacecraft was located upstream in the solar wind at the time of the shock impact. To study the magnetosphere response GOES-13, GOES-15, LANL-97A, THEMIS, and Cluster spacecraft are used.

The Wind Magnetic Field Investigation (MFI) instrument, consisting of two flux-gate magnetometers, was used for IMF observations (Lepping et al. 1995). The Wind Solar Wind Experiment (SWE) Faraday Cup - Ion Data was used to obtain information on solar wind plasma conditions (Ogilvie et al. 1995). We use the MAGNETOMETER (MAG) and MAGnetospheric Electron Detector (MAGED) instrument on GOES-13 and 15 to understand the response at geosynchronous orbit (Hanser 2011; Rodriguez et al. 2014). MAGED is a set of nine collimated solid state detectors, data are provided as differential

electron fluxes for 40, 75, 150, 275, and 475 keV midpoint energies from nine telescopes. The Synchronous Orbit Particle Analyser (SOPA) on the Los Alamos space environment monitor LANL-97A in geosynchronous orbit ( $\sim 6.6 R_E$ ), is used to study electron and proton intensities in the nightside geosynchronous orbit. SOPA measures electrons in nine electron channels from  $\sim 0.05$ – $1.5$  MeV and protons from  $\sim 0.2$ – $2.5$  MeV. Note that neither LANL-97A nor any other LANL space environment monitor carries any magnetometers (Taylor et al. 2004). The THEMIS Solid State Telescope (SST) records ions and electrons within the energy range from 25 keV to 6 MeV. The Flux Gate Magnetometer (FGM) on THEMIS measures the background magnetic field in the near-Earth space environment (Angelopoulos 2009; Auster et al. 2008). The measurements of the IMF, solar wind parameters, and magnetospheric particle and field with one-minute cadence were utilized for the current study.

Figure 1 shows IMF and solar wind parameters for the studied event. The top panel in the figure shows the total IMF strength (IMF,  $B_t$ ) and its components ( $B_x$ ,  $B_y$ ,  $B_z$ ). At the 21:09 UT shock onset, IMF  $B_z$ , thermal speed ( $V_{th}$ ) and the solar wind particle density ( $N_p$ ) decreased sharply, whereas the solar wind bulk ( $V_{sw}$ ) shows the increase. These observed changes in the solar wind parameters clearly indicate the shock is an FRS. The shock speed is estimated using the Rankine–Hugoniot equations in the reference system with an origin at the shock. The Rankine–Hugoniot equations, based on assumptions of energy and momentum conservation across the shock front (Landau & Lifshitz 1960; Tsurutani et al. 2011; Oliveira 2017) yield the values  $590 \text{ km s}^{-1}$  and  $\sim 10^\circ$  for the shock speed relative to the Earth and shock impact angle, respectively. Here, shock impact angle is the angle made by IP shock normal with the Sun–Earth line. The bottom panel of the figure shows SYM-H index, a measure of the global averaged; low latitude magnetic field response on the ground. The SYM-H index shows a decrease of about 20 nT around 21:54 UT which is consistent with the expected solar wind flow time  $\sim 45$  min from Wind’s upstream location ( $X_{GSE} = 204.5 R_E$ ,  $Y_{GSE} = -89.5 R_E$ ,  $Z_{GSE} = -0.05 R_E$ ) to the Earth.

Figure 2(a) shows magnetospheric spacecraft positions for the event. GOES-15 was located near noon, GOES-13 and THEMIS-A were located near dusk, and LANL-97A was near midnight. The figure also shows the magnetopause boundary estimated by the Shue et al. (1998) magnetopause model just before (blue dashed curve) and just after (black solid curve) the shock impacted the magnetosphere. The shock wave front is shown as inclined dashed black lines. The left and right lines indicate the location of the shock front at the time of magnetopause impact and at the time of the maximum depression observed in SYM-H associated with the shock, i.e. after 10 min of shock onset, respectively. Note that the magnetosphere expands in response to the FRS impact, as opposed to the compression caused by the impact of an FFS, as shown in Figure 2 of Rudd et al. (2019).

### 3. Observations and Results

#### 3.1. Magnetic Field Response

Figure 2(b) shows the space-based and averaged global magnetic field response to this shock. The dashed vertical line indicates the onset of the FRS as seen in the magnetic field at GOES-15, GOES-13, THEMIS-A spacecraft, and in SYM-H

on the ground. A clear decrease is seen at all spacecraft and on the ground. The onset of the shock is seen earlier ( $\sim 21:50:00$ ) at GOES-15, later at GOES-13 ( $\sim 21:52:00$ ), and still later on the ground ( $\sim 21:53:00$ ). Timing analysis using GOES-15, GOES-13, and SYM-H index data indicates that the rarefaction front moved through the magnetosphere with an antisunward speed of  $\sim 209$ – $232 \text{ km s}^{-1}$ . The observed speed is consistent with the reported speed of  $\sim 300 \text{ km s}^{-1}$  for an SI<sup>−</sup> by Araki & Nagano (1988). THEMIS-A shows a gradual decrease in the magnetic field strength but the onset time is not very clear. After the onset of the shock observed at GOES-15 the magnetic field reaches a minimum in 10 minutes and after that almost remains steady. Unlike GOES-15, GOES-13 shows a steady decrease in magnetic field strength after the onset and the magnetic field continued to decrease. A clear local time dependence can be observed by comparison of the magnetic field profiles of GOES-15 and GOES-13. Note that around 21:30 UT, prior to the FRS onset as seen at GOES-13, -15 and SYM-H, there is a sharp enhancement in the magnetic field which could be due to a small density jump around 20:30 UT seen at Wind.

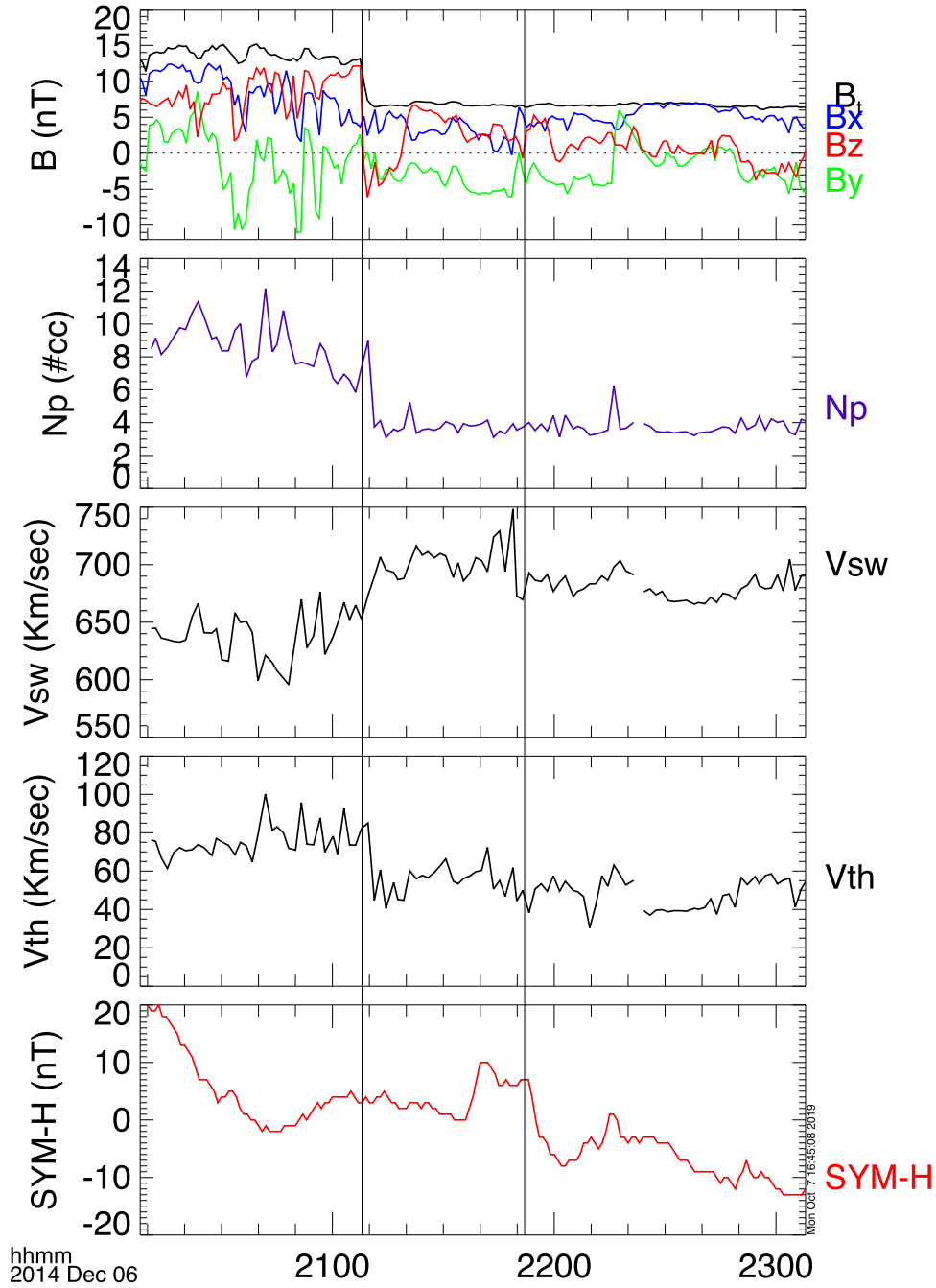
#### 3.2. GOES Particle Flux Response

Figure 3 shows GOES-15, 13 electron fluxes. The vertical line indicates the onset of the shock at each spacecraft as identified in Figure 2. A decrease in electron flux for selected channels follows the rarefaction-induced magnetic field for the FRS duration. The following general characteristics can be readily noted based on observed signatures: (1) an almost instantaneous decrease is observed in most of the electron flux channels; (2) there is no indication of any dispersive effect over the entire spectral range as all the channels which show the signature show a decrease at the same time; (3) low energy (40–75 keV) particle fluxes follow the magnetic field variations quite well.

However, close observation reveals strong energy dependent effects leading to significantly different signatures in the various energy channels. The lower energy channels show a rapid decrease as compared to the higher energy channels, which show weak or almost unidentifiable signatures. The signals at higher energies could be smeared out in time due to the fast drift rate superposing the time and spatial-variation. Note that all electron fluxes show sharp changes around 21:30 UT prior to the FRS onset which could be associated with a small pressure jump around 20:30 UT observed by Wind. This is also evident in the GOES magnetic field and it is manifested as a sharp increase in SYM-H around 21:35 UT. Curiously, the flux profile seen in the 75 keV channel of GOES-13 is very well correlated with the magnetic field variation seen by GOES-15. The percentage change in intensity for the different energy channels varies. For the 75 keV channel more than a 70% decrease was recorded by GOES-13. The proton data were absent for both the spacecraft.

Pitch angle distributions at various energies were examined. Intensities at all pitch angles decrease after the shock impact at both spacecraft. Figure 4 shows near-field-aligned ( $\sim 30^\circ$ ) and perpendicular ( $\sim 90^\circ$ ) electron fluxes of 75 keV electrons. Just prior to the shock arrival field-aligned intensities were greater than those for the equatorially trapped particles, in contrast to the nominal distribution. The anisotropy index ( $A$ ) was calculated for both spacecraft, where  $A = [j(90^\circ) - j(30^\circ)] / [j(90^\circ) + j(30^\circ)]$ . The value of  $A$





**Figure 1.** Solar wind parameters observed by Wind during the FRS on 2014 December 6. The onset of the shock at Wind is shown by left vertical line and the right vertical line shows the onset of the shock at the ground as seen in the SYM-H index.

was negative prior to the onset of the FRS, and as an immediate response became less negative or even positive. After the shock  $A$  remained close to zero, i.e almost isotropic distributions were observed. All other energies show a similar effect (not shown here). This implies that the particle population residing radially inward had an almost isotropic pitch angle distribution and that these particle populations moved to the spacecraft due to an expansion of the magnetosphere. Asymmetric or butterfly distributions are more commonly observed in the outer magnetosphere or higher L-shells than in the inner magnetosphere (Ni et al. 2016). Therefore, during the expansion of the magnetosphere caused by the FRS, a spacecraft could observe a decrease in anisotropy as the spacecraft encounters particles

from the inner magnetosphere, i.e as the distribution shifts from butterfly-like to one that is more isotropic.

### 3.3. LANL Particle Intensities Response

Figure 5 shows the electron and proton fluxes observed by the LANL-97A spacecraft, located near midnight. A very strong and clear response is observed at this spacecraft in both the electron ( $\sim 1-9$  MeV) and proton ( $\sim 0.2-0.9$  MeV) fluxes. The observed decrease is non-dispersive as the onset is seen simultaneously in all the energy channels. Interestingly, even MeV electrons show the decrease in intensity at the onset time. The overall percentage of the decrease is  $\sim 70\%$  for each

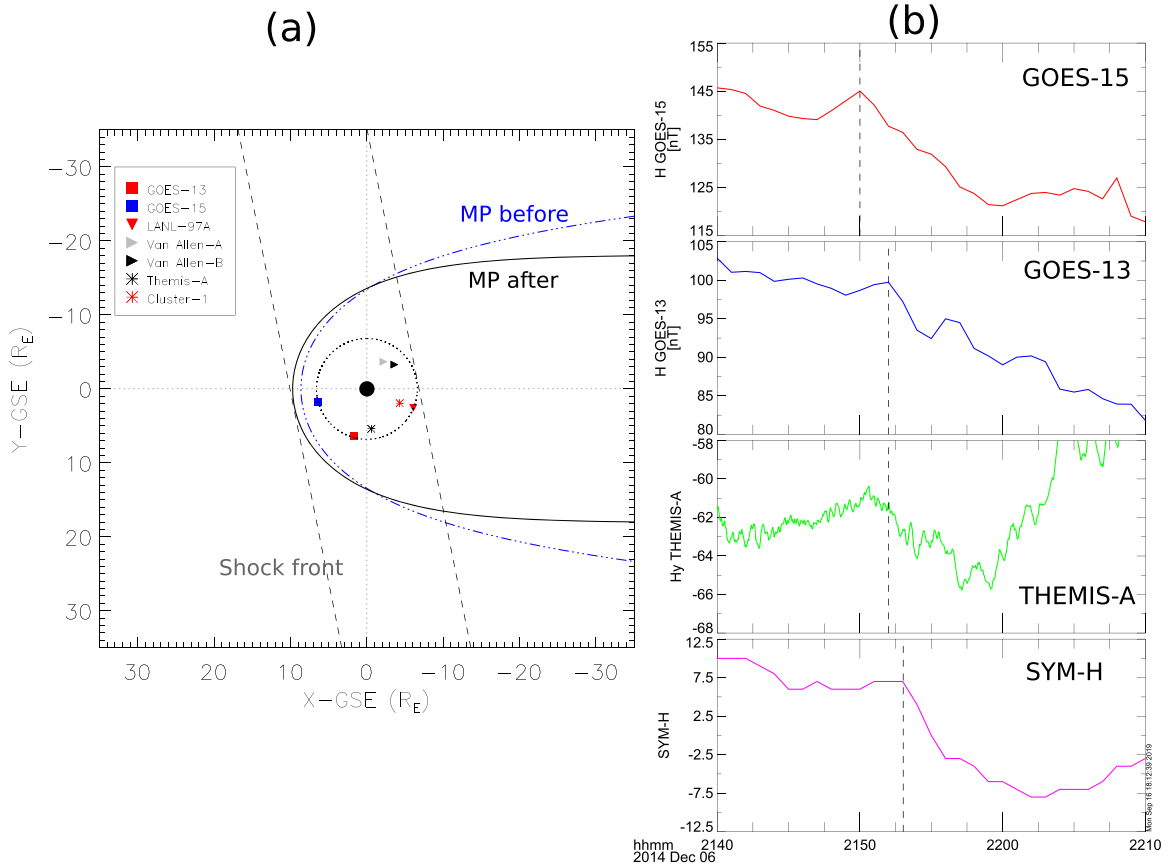


**Figure 2.** (a) Spacecraft positions during the FRS event of 2014 December 6 at 21:50 UT. The magnetopause shapes just prior to (blue dashed line) shock arrival and at the shock onset (black solid line) are shown. Dotted circle shows geosynchronous orbit. (b) Magnetic field variation caused by the FRS event of 2014 December 6. The dashed vertical lines represent onset of the FRS as seen at the respective spacecraft. Total magnetic field of GOES is shown in top two panels. Third panel from top shows  $y$ -component of magnetic field as recorder by THEMIS-A. Note that the  $y$ -component of the magnetic field ( $H_y$ ) for THEMIS-A, is shown as other components did not show any clear variation. At the bottom global low latitude average geomagnetic field response is shown by the SYM-H index.

electron channel and  $\sim 47\%$  for each proton channel which showed the signature.

As shown in Figure 5 bottom panel, before and after electron spectra of electrons show that the spectral slope does change after the onset of the shock. The observed spectral slope for electrons is  $\sim 3.6$  prior to the shock but has steepened to  $\sim 4.1$  after the shock. The change in slope value is more than the error, indicating that the observed change is real and significant. The implications of this will be discussed in Section 5.

#### 4. Model Comparisons

We use magnetospheric models to simulate the global response of the magnetosphere to the FRS and for comparison with the spacecraft observations. They can provide magnetic field responses at locations where no spacecraft observations exist.

The Block-Adaptive-Tree-Solarwind-Roe-Upwind-Scheme BATS-R-US (Ridley & Liemohn 2002; Tóth et al. 2005, 2012) was used in the present study. This model was developed by the Computational Magnetohydrodynamics (MHD) Group at the University of Michigan and is now available as part of the Space Weather Modeling Framework (SWMF). The model run for the shock event was carried out at the Community Coordinated Modeling Center (CCMC). BATS-R-US has been used to investigate the interaction of IP shocks with the Earth's magnetosphere by many studies

(Koval et al. 2006; Ridley et al. 2006; Samsonov et al. 2007; Samsonov & Sibeck 2013; Samsonov et al. 2015).

Solar wind plasma parameters (density, velocity, temperature) and IMF observed by the Wind spacecraft are inputs to the model. The solar wind data is transformed into GSM coordinates and propagated from Wind's position to the sunward boundary of the simulation domain. The Earth's magnetic field is approximated by a dipole and the dipole orientation updated during the simulation period. Outputs of the run are magnetospheric plasma parameters including density, pressure, velocity, magnetic field, and electric currents.

Figure 6 shows simulated densities in the equatorial plane of the magnetosphere before (left top panel) and after (right top panel) the shock arrival. The simulation reproduces the clear reduction in particle number density at geosynchronous orbit, an expected FRS impact signature. The model time series for the magnetic field ( $B$ ) and pressure ( $P$ ) variations at the location of GOES-15 and LANL-97A are shown in the lower panels. On the dayside the GOES-15 modeled-pressure shows a clear step-like pressure drop, whereas the pressure decrease at LANL-97A is gradual. The model predicts a step-like decrease of  $\Delta B \sim 25$  nT at GOES-15, with the magnetic field remaining low after the shock. Overall, the model fields agree with GOES-15 observations to a reasonable degree. The modeled magnetic field at LANL-97A shows a decrease in  $B$  of just 6 nT, very small compared to that at GOES-15. There are no magnetic field measurements available from LANL-97A. So

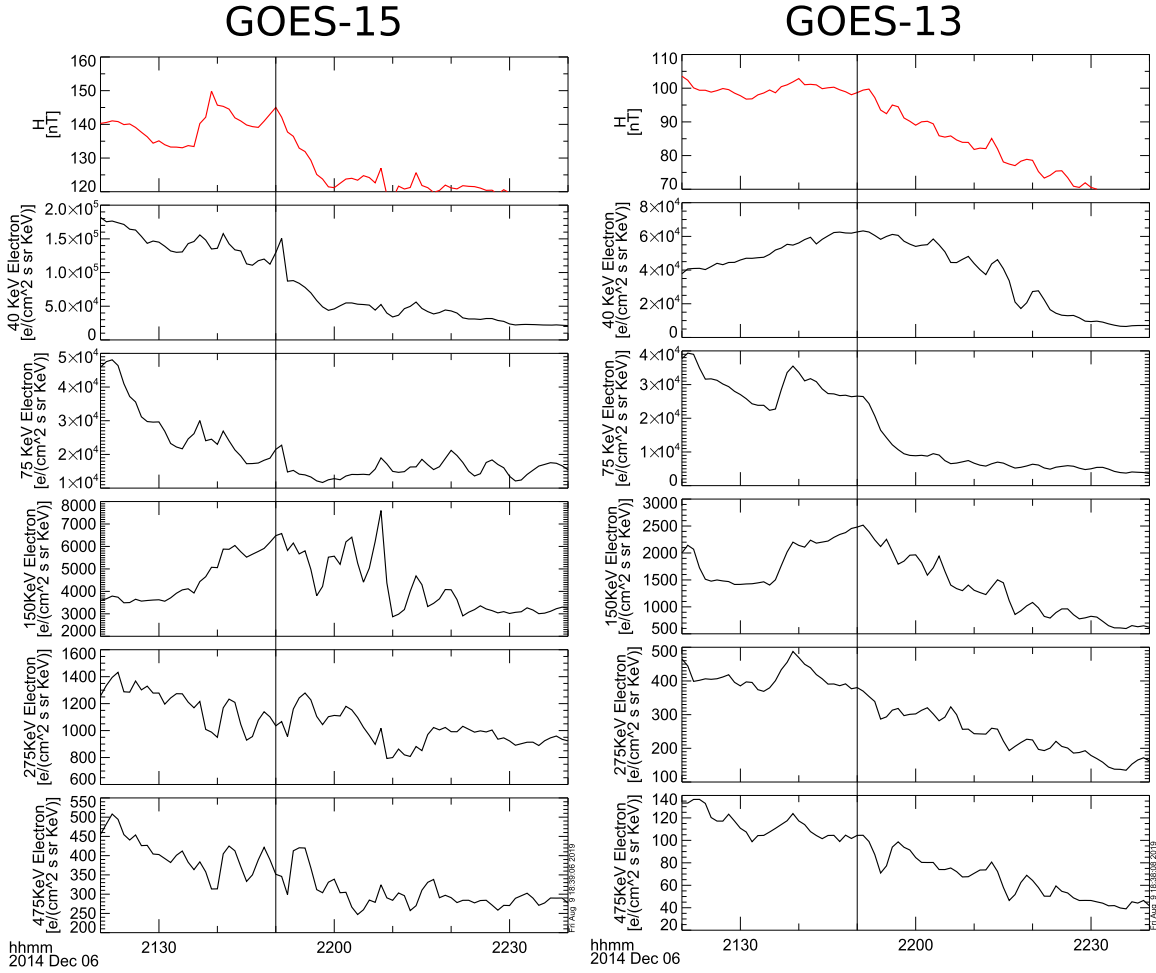


**Figure 3.** Electron flux response to the FRS as observed by GOES-13, -15. The vertical line indicates the onset of FRS signature as seen in magnetic field variations measured by GOES-15. There is steady decrease in magnetic field at GOES-13 unlike GOES-15. The low energy particles show FRS signature, whereas there is no clear signature at higher energies at both the spacecraft.

this model predication cannot be validated using LANL-97A. Thus to validate the nightside model fields, we have compared its predictions to the Cluster spacecraft observations (not shown here) which were taken in the nightside. The decrease of  $\Delta B \sim 15$  nT is observed by all four spacecraft. However, the BATS-R-US model predicts only  $\sim 6$  nT variation at this location. This indicates that the model underestimates magnetic field values on the nightside. Therefore, it is likely that it also under-predicts magnetic field variations at LANL-97A and thus underestimates the adiabatic effect. The following section tries to quantify the contribution of adiabatic and other effects to the observed particle intensity variations.

## 5. Contribution of Adiabatic Effects and Radial Gradients

The variations in the particle intensities attending the shock arrival could result from any combination of (1) advected radial gradients, (2) adiabatic effects, (3) spectral changes, and other (4) non adiabatic processes. From Wilken et al. (1986) the observed change in the flux ( $j$ ) to first order estimate can be expressed by the following equation, the first term represents the change due to adiabatic processes, whereas the second term represents the changes associated with advected radial

gradients in the particle intensities.

$$\Delta j(E = \text{const}) = \frac{\delta j}{\delta B} \Delta B + \frac{\delta j}{\delta R} \Delta R, \quad (1)$$

where  $\Delta B$  and  $\Delta R$  represent the changes in magnetic field strength and radial position seen by the magnetosphere plasma population. If we assume the first invariant and phase space density are conserved during the transient rarefaction of the magnetosphere, this relationship can be expressed as

$$\frac{\Delta j}{j(E)} = \frac{\Delta B}{B_0} (\gamma_0 + 1) + \frac{\Delta k}{k_0} + \frac{\Delta \gamma}{\gamma_0} \ln \left( \frac{j_0}{k_0} \right) \quad (2)$$

Here, the first term represents the change due to adiabatic processes, whereas the second term represents the changes associated with radial gradients and the third due to change in spectral properties of the particle population. We have attempted to evaluate each term of this expression using THEMIS-A particle data. The orbit of THEMIS-A crossed a wide range of L-shells which enables estimation of gradients in particle intensity and spectral index. These gradients are estimated around geosynchronous orbit prior to the onset of the shock. Figure 7(a) shows the electron flux data in nine energy channels utilized for the estimates. Note that the higher

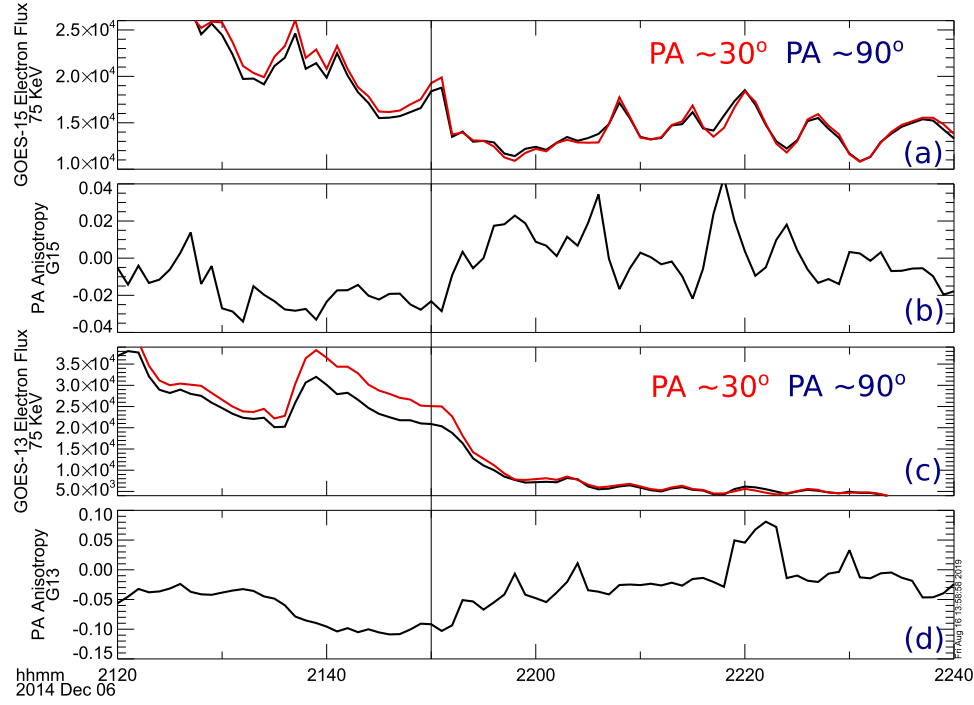


**Figure 4.** Field-aligned ( $PA \sim 30^\circ$ ) and perpendicular ( $PA \sim 90^\circ$ ) pitch angle Electron flux response to the FRS as observed by GOES-13, -15 for the 75 keV channel

fluxes are observed at lower L-shells for these energies and locations. The flux measurements are used to calculate radial gradients in flux and spectral index.

Thus, the various terms of Equation (2) are calculated based on these measurements. Since there are no magnetic field measurements onboard LANL-97A to estimate the adiabatic term, magnetic field observations by Cluster spacecraft  $\Delta B = 15$  nT and  $B_0 = 100$  nT were used. By using the TS04 model the magnetic foot points are estimated for *pres*shock and *post*shock solar wind dynamic pressure conditions to deduce a  $\sim 0.5 R_E$  expansion of the magnetosphere at geosynchronous orbit, thus  $\Delta R$  was taken as  $0.5 R_E$ .

Figure 7(b) shows values for each term in Equation (2) for several energies. The total fractional change  $\left(\frac{\Delta j}{j_0}\right)$  is also presented to see the net estimate of the decrease in the various energy channels. The adiabatic  $\left(\frac{\Delta B}{B_0}(\gamma_0 + 1)\right)$  and spectral gradient  $\left(\frac{\Delta \gamma}{\gamma_0} \ln\left(\frac{j_0}{k_0}\right)\right)$  terms are the dominant contribution to the observed decrease. Advection of the negative radial gradients  $\left(\frac{\Delta k}{k_0}\right)$  in intensity make only negligible positive contributions to the particle intensity. The calculated total fractional decrease  $\left(\frac{\Delta j}{j_0}\right)$  for 100 keV and above energies is  $< -0.5$  reaches almost  $-0.8$  for 700 keV energy. This estimate is comparable to that observed. The observed fractional flux decrease at LANL-97 for  $\sim 1122$  keV is  $-0.75$ . Whereas, at GOES-13 for 75 keV electrons the observed fractional decrease is  $-0.71$  which is very close to the estimate of  $-0.69$ . Note that these estimates are done using observed magnetic field, spectral slope, and particle intensity gradients and remarkably we do get a close match with the observed fractional changes in the particle intensities.

## 6. Role of Shock Impact Angle

Van Allen Probes were located deep within the post midnight magnetosphere and did not see any significant variation in particle intensities or magnetic field. This could be due to a subdued response of magnetosphere to the shock at lower L-shells. Also, the magnetosphere might respond asymmetrically to an interplanetary shock depending on the angle of shock impact (Oliveira & Raeder 2015; Vichare et al. 2014; Oliveira & Samsonov 2018; Rudd et al. 2019). The shock was slightly inclined, and first impacted the magnetosphere on the afternoon side which also could contribute to a weak or absent shock impact at the Van Allen Probes location.

In order to infer the shock inclination influence we have used the Partial Ring current local time SMR index. SuperMAG partial ring current index (SMR) is similar to the SYM-H index but computed by a higher number of ground magnetometers (Newell & Gjerloev 2012). Figure 8 shows the various local time SMR indices. Four equally sized local time sectors are defined with centers at 00, 06, 12, and 18 MLT to compute the local time SMR which are shown in the figure. The maximum decrease is observed in the noon sector, whereas the minimum is seen in the dawn sector. The second strongest response is seen near the *dusk-midnight* sector. This implies that there is a strong local time dependence of the ground-based magnetic field response due to an asymmetric rarefaction of the magnetosphere. The Van Allen Probes were located in the dawnside magnetosphere where the shock impact was weaker due to its inclination. Thus an asymmetric expansion of the magnetosphere could explain the observed varied response of the particles to the *shock* versus local time.

## 7. Discussion and Conclusions

The present study shows that not only FFSs, but also FRSs, generate interesting dynamics. The geosynchronous response is



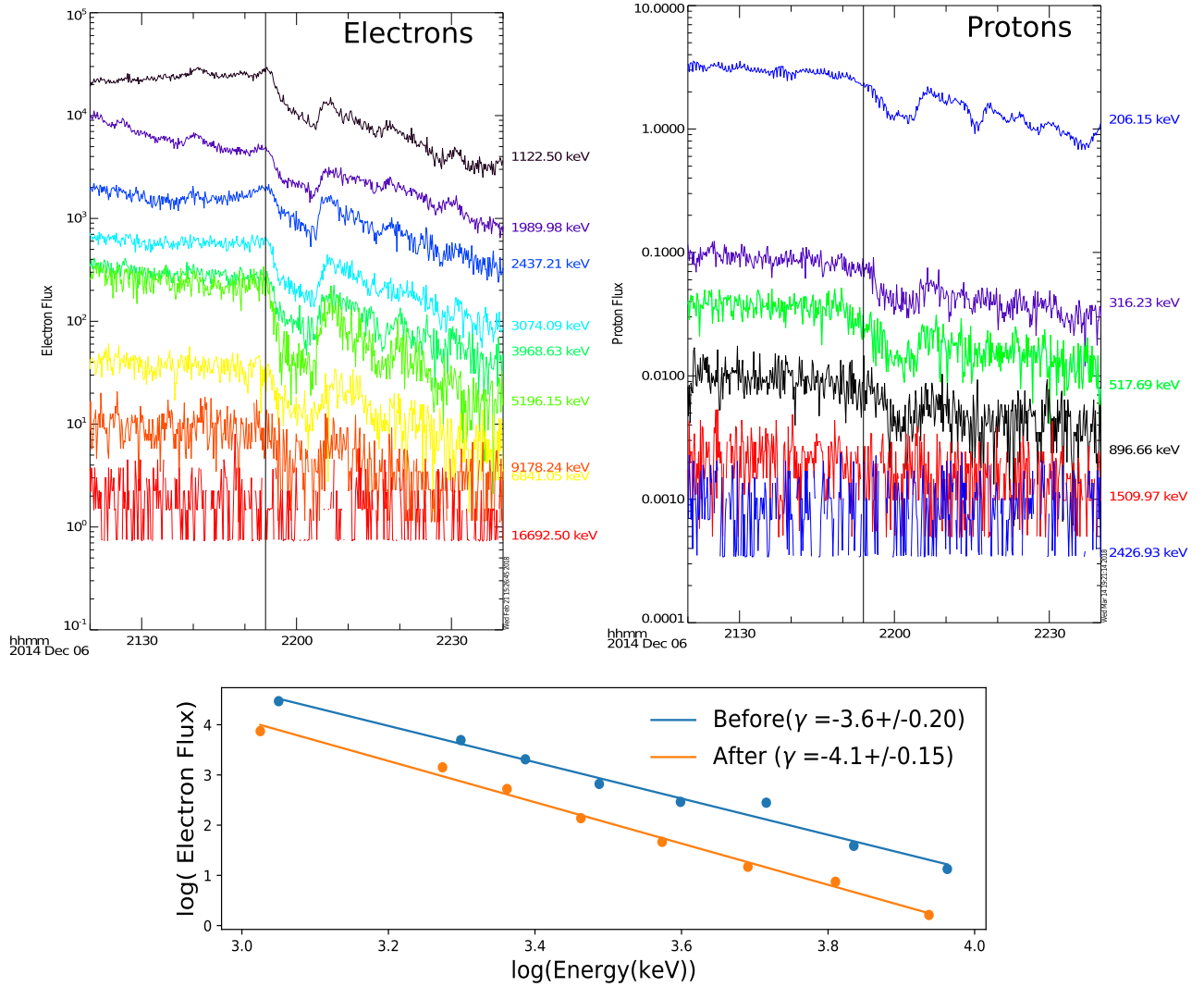


**Figure 5.** Electron (left panel) and proton (right panel) flux response to FRS as observed by LANL-97A. The vertical line indicates the onset of the FRS signature as seen in particle intensities which coincide with the onset observed in the SYM-H index. Energy spectra of high energy electrons observed by LANL-97A (bottom panel) in night sector before and after the shock onset.

investigated using GOES-13, -15, and LANL-97A spacecraft data. The magnetic field strength decreases at geosynchronous orbit and on the ground in response to the inclined FRS. The SYM-H index dropped by  $\sim 20$  nT. The timing analysis shows that the rarefaction wave front propagated antisunward at  $209\text{--}232\text{ km s}^{-1}$ . The particle response also seems to be global in nature as most electron energy channels from 10 s of keV to MeV energies show a decrease in intensity. However, not all the energy channels show the same relative decrease or variation in magnitude. It is possible that gradient and betatron effects counterbalance each other, resulting in the absence or small size of the signature or its absence in different energy channels which we have attempted to address here. The shock impact not only caused a decrease in particle intensities but also in pitch angle anisotropy. This implies that those particle populations which advected outward through geosynchronous orbit due to the shock-induced magnetospheric expansion had an almost isotropic pitch angle distribution.

To identify the contribution of radial gradient and adiabatic effects to the observed decrease we followed the formalism of Wilken et al. (1986). Moreover, the required magnetic field to

carry out this calculation was inferred using the BATS-R-US model at the LANL-97 A location. However, when we validated the model outputs using the Cluster spacecraft magnetometer data we found that the model underestimated perturbations in the nightside magnetic field. Our first order estimate following Wilken et al. (1986), and using THEMIS-A showed that the radial gradient makes only a small contribution. The work by West et al. (1973) and West (1979) shows that the radial gradient of fluxes at constant energy tends to assume small values for low energy ( $< 200$  keV) electrons and increase monotonically for higher energies. Our first order estimate following the Wilken et al. (1986) approach agrees with this, i.e. the radial gradient values are very small ( $\sim 0$ ) for keV electrons. Further, we find that the adiabatic and spectral terms significantly contribute to the observed decrease. The calculated contributions are consistent with the observed decrease in electron intensities at GOES-15, -13 and LANL-97A spacecraft.

The shock impact on the magnetosphere was slightly inclined, resulting in an asymmetric expansion of the magnetosphere. This is well shown by variations in the SMR index at

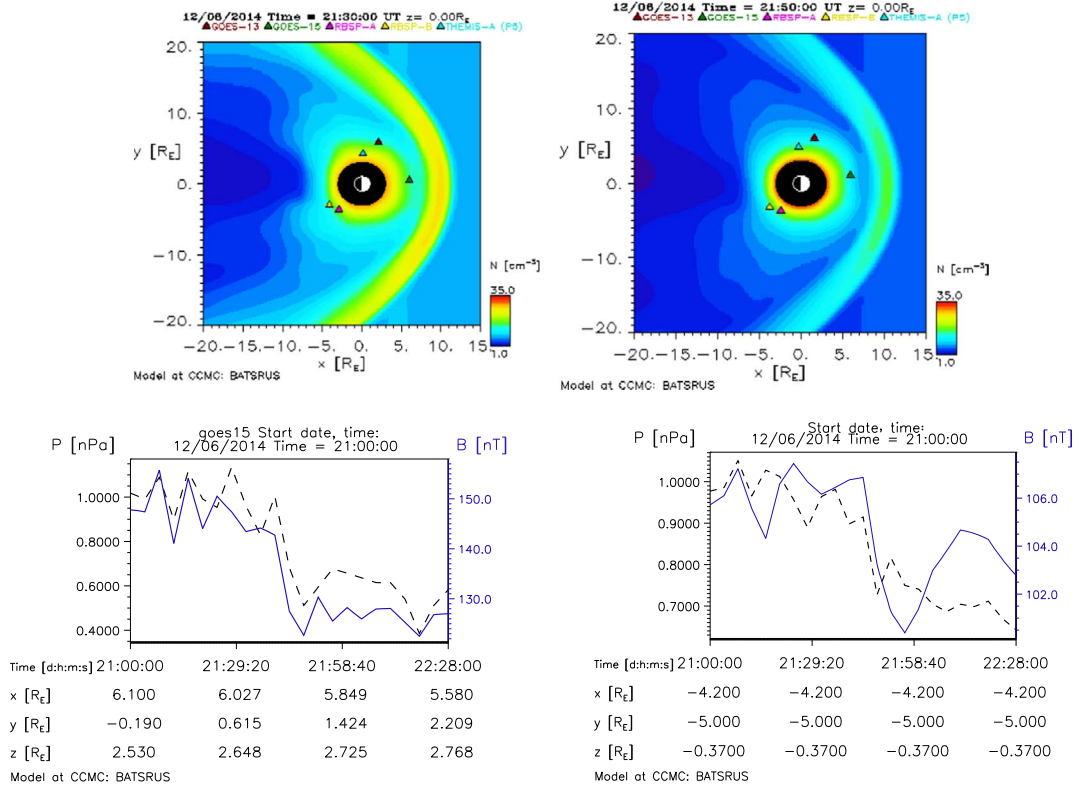


**Figure 6.** BATS-R-US model outputs for the studied event. Top panels are magnetosphere density profiles in the equatorial plane. Bottom panels are time series outputs of pressure and magnetic field at GOES-15 and LANL-97A locations.

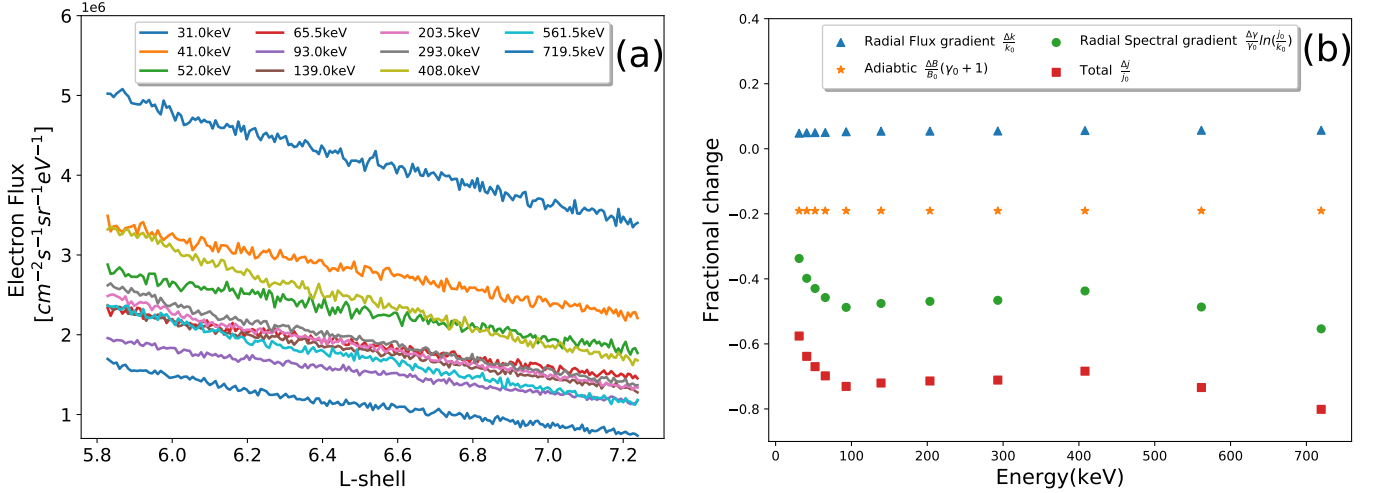


**Figure 7.** (a) The L-shell variation of electron fluxes as observed by THEMIS-A during inbound 11:03 to 11:13 UT on 2014 December 6th. (b) Estimated contribution of various terms associated with radial gradients and adiabatic effect in the observed decrease using THEMIS-A data. The red squares represent the net contribution of all three terms.

different local times. Spacecraft to spacecraft variations in the response at different local times could be explained by the inclined incidence of the shock. This highlights the importance of the shock impact angle during shock interaction with the magnetosphere and is consistent with the earlier reports, as shown by simulations (Guo et al. 2005; Oliveira & Raeder 2014; Samsonov et al. 2015) and observations (Takeuchi et al. 2002b; Wang et al. 2006; Oliveira et al. 2016, 2018).

The adiabatic effect underlying the observed decrease in relativistic electron intensities can be understood as follows. The onset of the FRS causes the magnetosphere to expand,

relativistic electrons conserving their third invariant move radially outward to compensate for the reduced local magnetic field strength. Thus LANL-97 which is almost located at fixed radial distance then measures the intensity of electrons previously present at lower L-shells. The outward moving electrons experience a weaker magnetic field and to conserve the first adiabatic invariant ( $\mu$ ), their perpendicular energy must decrease. Therefore, the distribution of electrons shifts to lower energy. A spacecraft measuring flux at fixed energy,  $E_0$  and fixed radial distance measures the flux of electrons initially at a lower L-shell shifted to lower energies. Thus generally this

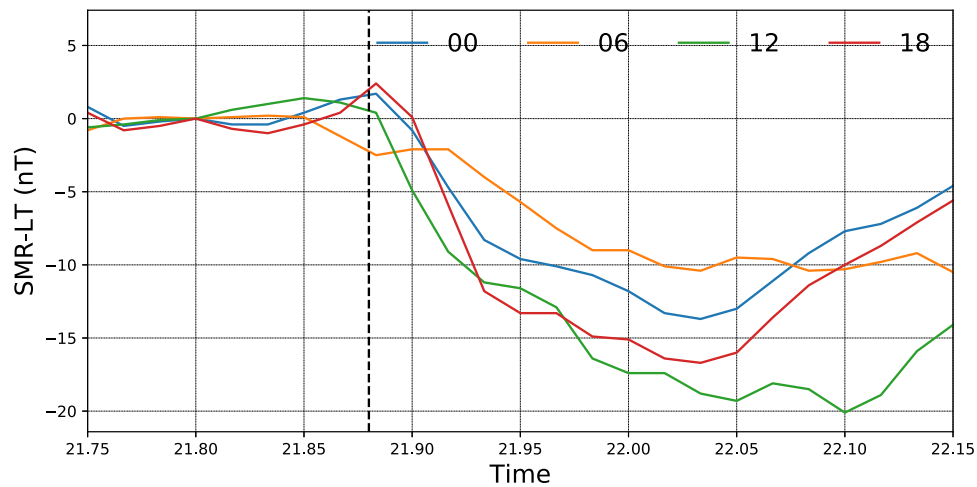


**Figure 8.** Local time SMR indices during the event. The vertical dotted line represents the onset of the FRS, whereas, the curves denote the local time SMR index at various local times. A strong local time dependence of the magnetic field decrease is associated with FRS.

outward movement results in a decrease of electron intensity at fixed energy for a decrease in magnetic field strength. In addition to this effect, if the preshock magnetosphere had a strong gradient in spectral slope, even this also can contribute to the decrease. The dominance of the estimated spectral term supports this. These two effects are primarily responsible for the observed decrease in particle fluxes caused by the FRS on 2014 December 6.

Note that the magnetosphere responds differently to interplanetary FFSs and FRSs. The FFS compresses the magnetosphere, whereas the FRS causes an expansion of the magnetosphere. The present study shows that the reverse shock predominantly caused the decrease in particle intensities. However, particle responses depend on magnetospheric conditions prior to the onset of the shock such as radial gradients in intensities and spectral index and could manifest as no effect or even enhancements during either fast forward or fast reverse shock. Even though FRSs are rare, a statistical study would shed light on the general response of magnetosphere particles to FRS. Moreover, the findings of the study have implications to understand the interaction of shocks with the other planetary magnetospheres.

The solar wind parameters, interplanetary magnetic field and geomagnetic indices used in this study are obtained from CDAWEB (<https://cdaweb.gsfc.nasa.gov/>) and SUPERMAG (<http://supermag.jhuapl.edu/>). We thank Wind, GOES, THEMIS, Cluster teams for providing the data. The modeling part of the work was carried out using the SWMF/BATSRUS tools developed at The University of Michigan Center for Space Environment Modeling (CSEM) and made available through the NASA Community Coordinated Modeling Center (CCMC). Also, we thank Community Coordinated Modeling Center (CCMC, Run Number [Ankush\\_Bhaskar\\_051118\\_1](#)) for running the required models for this work. We thank Vassilis Angelopoulos, UCLA and Brian Kress, NOAA for valuable discussions. This work is carried out under NASA Living With a Star Jack Eddy Postdoctoral Fellowship Program, administered by UCAR's Cooperative Programs for the Advancement of Earth System Science (CPAESS). A.B thanks UCAR, CPAESS, and NASA/GSFC for providing excellent facilities and environment for the work. Some work at NASA/GSFC was funded by the Van Allen Probes mission.

## ORCID iDs

Ankush Bhaskar <https://orcid.org/0000-0003-4281-1744>  
Geoffrey Reeves <https://orcid.org/0000-0002-7985-8098>

## References

- Akasofu, S.-I. 1964, *P&SS*, **12**, 573  
Alves, M. V., Echer, E., & Gonzalez, W. D. 2011, *JASTP*, **73**, 1380  
Andrioli, V. F., Echer, E., Savian, J. F., & Schuch, N. J. 2006, *Revista Brasileira de Geofísica*, **25**, 175  
Angelopoulos, V. 2009, In *The THEMIS mission* (Berlin: Springer), 5  
Araki, T. 1994, in *Solar Wind Sources of Magnetospheric Ultra-Low-Frequency Waves*, Geophysical Monograph Series, **Vol. 81**, ed. M. J. Engebretson et al. (Washington, D.C: American Geophysical Union), 183  
Araki, T., Fujitani, S., Yumoto, K., et al. 1997, *JGR*, **102**, 14075  
Araki, T., & Nagano, H. 1988, *JGRA*, **93**, 3983  
Auster, H., Glassmeier, K., Magnes, W., et al. 2008, *SSRv*, **141**, 235  
Burguess, D. 1995, in *Introduction to Space Plasma Physics*, ed. M. G. Kivelson & C. T. Russell (Cambridge: Cambridge Univ. Press)  
Burlaga, L. F. 1971, *SSRv*, **12**, 600  
Burlaga, L. F. 1995, *Interplanetary Magnetohydrodynamics* (New York, NY: Oxford Univ. Press)  
Cavus, H., Araz, G., Caglar Coban, G., Rahee, A., & Karafistan, A. I. 2019, *AdSpR*, **63**  
Echer, E., Alves, M. V., & Gonzalez, W. D. 2004, *SoPh*, **221**, 361  
Echer, E., Gonzalez, W. D., Dal Lago, A., et al. 2005, *AdSpR*, **36**, 2313  
Echer, E., Gonzalez, W. D., Vieira, L. E. A., et al. 2003, *BrJPh*, **33**, 115  
Guo, X.-C., Hu, Y.-Q., & Wang, C. 2005, *ChPhL*, **22**, 3221  
Hajra, R., & Tsurutani, B. T. 2018, *ApJ*, **858**, 123  
Hajra, R., Tsurutani, B. T., & Lakhina, G. S. 2020, *ApJ*, **899**, 3  
Hanser, F. 2011, *EPS/HEPAD calibration and data handbook* (Tech. Rep. GOES-ENG-048D) (Carlisle, MA: Assurance Technology Corporation)  
Hudson, M., Kotelnikov, A., Li, X., et al. 1995, *GeoRL*, **22**, 291  
Huttunen, K. E. J., Slavin, J., Collier, M., et al. 2005, *AnGeo*, **23**, 609  
Joselyn, J. A., & Tsurutani, B. T. 1990, *Eos Transactions AGU*, **71**, 1808  
Kanekal, S., Baker, D., Fennell, J., et al. 2016, *JGRA*  
Kilpua, E. K. J., Lumme, E., Andréevová, K., Isavnin, A., & Koskinen, H. E. J. 2015, *JGRA*, **120**, 4112  
Koval, A., Šafránková, J., Němeček, Z., et al. 2006, *GeoRL*, **33**  
Landau, L. D., & Lifshitz, E. M. 1960, *Electrodynamics of continuous media* (Oxford, UK: Pergamon Press)  
Lepping, R., Acuña, M., Burlaga, L., et al. 1995, *SSRv*, **71**, 207  
Li, X., Roth, I., Temerin, M., et al. 1993, *GeoRL*, **20**, 2423  
Looper, M., Blake, J., Mewaldt, R., Cummings, J., & Baker, D. 1994, *GeoRL*, **21**, 2079  
Mullen, E., Gussenhoven, M., Ray, K., & Violet, M. 1991, *ITNS*, **38**, 1713  
Newell, P., & Gjerloev, J. 2012, *JGRA*, **117**  
Ni, B., Zou, Z., Li, X., et al. 2016, *GeoRL*, **43**, 544  
Ogilvie, K. W., Chornay, D. J., Fritzenreiter, R. J., et al. 1995, *SSRv*, **71**, 55  
Oliveira, D. M. 2017, *BrJPh*, **47**, 81

- Oliveira, D. M., Arel, D., Raeder, J., et al. 2018, *SpWea*, **16**, 636
- Oliveira, D. M., & Raeder, J. 2014, *JGRA*, **119**, 8188
- Oliveira, D. M., & Raeder, J. 2015, *JGRA*, **120**, 4313
- Oliveira, D. M., Raeder, J., Tsurutani, B. T., & Gjerloev, J. W. 2016, *BrJPh*, **46**, 97
- Oliveira, D. M., & Samsonov, A. A. 2018, *AdSpR*, **61**, 1
- Patel, V. L., & Coleman, P. J. 1970, *JGR*, **75**, 7255
- Richter, A. K., Hsieh, K. C., Luttrell, A. H., Marsch, E., & Schwenn, R. 1985, in *In Collisionless Shocks in the Heliosphere: Reviews of Current Research*, Geophysical Monograph Series, Vol. 35, ed. B. T. Tsurutani & R. G. Stone (Washington, D.C: American Geophysical Union), 33
- Ridley, A., & Liemohn, M. 2002, *JGRA*, **107**, ~~SMP~~
- Ridley, A. J., De Zeeuw, D. L., Manchester, W. B., ~~ans~~ensen, K. C. 2006, *AdSpR*, **38**, 263
- Rodriguez, J., Krossschell, J., & Green, J. 2014, *SpWea*, **12**, 92
- Rudd, J. T., Oliveira, D. M., Bhaskar, A., & Halford, A. J. 2019, *AdSpR*, **63**, 317
- Russell, C. T., Ginskey, M., & Petrinec, S. M. 1994a, *JGR*, **99**, 253
- Russell, C. T., Ginskey, M., & Petrinec, S. M. 1994b, *JGR*, **99**, 13
- Samsonov, A. A., Sergeev, V. A., Kuznetsova, M. M., & Sibeck, D. G. 2015, *GeoRL*, **42**, 4716
- Samsonov, A. A., & Sibeck, D. G. 2013, *JGR*, **118**, 3055
- Samsonov, A. A., Sibeck, D. G., & Imber, J. 2007, *JGR*, **112**, 1
- Schiller, Q., Kanekal, S., Jian, L., et al. 2016, *GeoRL*, **43**, 12
- Shen, X., Shi, Q., Zong, Q.-G., et al. 2017, *JGRA*, **122**, 1658
- Shue, J.-H., Song, P., Russell, C., et al. 1998, *JGRA*, **103**, 17691
- Siscoe, G. L., Formisano, V., & Lazarus, A. J. 1968, *JGR*, **73**, 4869
- Smith, E. J., Slavin, J. A., Zwickl, R. D., & Bame, S. J. 1986, in *In Solar Wind and Magnetosphere Coupling*, ed. Y. Kamide & J. A. Slavin (Tokyo, Japan: Terra Scientific), 345
- Smith, E. J., & Wolfe, J. H. 1976, *GeoRL*, **3**, 137
- Su, Z., Zhu, H., Xiao, F., et al. 2015, *GeoRL*, **42**, 3129
- Takeuchi, T., Araki, T., & Viljanen, A. 2002, *JGR*, **107**, 1096
- Takeuchi, T., Russell, C. T., & Araki, T. 2002, *JGR*, **107**, SMP 6
- Taylor, M., Friedel, R., Reeves, G., et al. 2004, *JGRA*, **109**
- Tóth, G., Sokolov, I. V., Gombosi, T. I., et al. 2005, *JGRA*, **110**, 70
- Tóth, G., Van der Holst, B., Sokolov, I. V., et al. 2012, *JCoPh*, **2**, 70
- Tsurutani, B., Smith, E., Pyle, K., & Simpson, J. 1982, *JGRA*, **87**, 7389
- Tsurutani, B., Zhou, X.-Y., Vasyliunas, V., et al. 2001, *SGeo*, **22**, 101
- Tsurutani, B. T., Gonzalez, W. D., Gonzalez, A. L., et al. 1995, *JGRA*, **100**, 21717
- Tsurutani, B. T., Lakhina, G. S., Verkhoglyadova, O. P., et al. 2011, *JASTP*, **73**, 5
- Vichare, G., Rawat, R., Bhaskar, A., & Pathan, B. M. 2014, *EP&S*, **66**, 1
- Wang, C., Li, C. X., Huang, Z. H., & Richardson, J. D. 2006, *GeoRL*, **33**, 1
- Wang, C., Li, H., Richardson, J. D., & Kan, J. R. 2010, *JGR*, **115**
- West, H., Buck, R., & Walton, J. 1973, *JGR*, **78**, 1064
- West, H. I., Jr 1979, *Quantitative Modeling of Magnetospheric Processes*, Geophys. Monogr. Ser. **21**, 150
- Wilken, B., Baker, D., Higbie, P., et al. 1986, *JGRA*, **91**, 1459
- Zhang, D., Liu, W., Li, X., et al. 2018, *GeoRL*, **45**, 7287
- Zhang, X. Y., Zong, Q.-G., Wang, Y. F., et al. 2010, *JGR*, **115**
- Zhou, X., & Tsurutani, B. T. 1999, *GeoRL*, **26**, 1097
- Zhou, X., & Tsurutani, B. T. 2001, *JGRA*, **106**, 18957

Q11

Q12